

Enhanced Oxygen Reduction Reaction Kinetics in Nanocrystalline IT-SOFC Cathodes

L. Baqué^{a,c}, A. Soldati^a, H. Troiani^a, A. Schreiber^b, A. Caneiro^a, and A. Serquis^a

^a CONICET, Centro Atómico Bariloche-CNEA, Av. Bustillo 9500, (8400) Bariloche, Argentina

^b Department of Chemistry and Physics of Geomaterials, Helmholtz-Zentrum Postdam, Germany

^c Present address: Department of Energy Conversion and Storage, Technical University of Denmark, DK-4000 Roskilde, Denmark

Solid oxide fuel cell performance is usually limited by high cathodic area specific resistance (ASR) at intermediate temperatures (500-700°C). ASR can be decreased by reducing particle size to nanometer range. This improvement is usually ascribed to the area/volume ratio increase and a higher concentration of active sites for the oxygen reduction reaction (ORR). Nevertheless, this solely explanation seems not to be enough for explaining the high electrochemical performance of some nanostructured $\text{La}_{0.4}\text{Sr}_{0.6}\text{Co}_{0.8}\text{Fe}_{0.2}\text{O}_{3-d}$ cathodes previously reported (Baqué et al., *Electrochemistry Comm.* 10 (2008) 1905-1908). Accordingly, the ORR of these cathodes was studied by electrochemical impedance spectroscopy (EIS) under air and under pure oxygen within the 400-700°C range. The nanostructure was characterized even at atomic level by transmission electron microscopy (TEM), revealing that the cathode is composed of nanocrystals surrounded by zones with some degree of crystalline disorder. These results suggest that this kind of nanostructure facilitate the ORR in this compound.

Introduction

Solid oxide fuel cells are environmental-friendly devices which can convert chemical energy from hydrogen and other fuels to electrical energy in a wide power range (1,2). The operation of these cells involves oxygen reduction at cathode, oxygen ions diffusion through electrolyte and fuel oxidation at anode. The development of thinner films with new compositions (such as gadolinium doped ceria) has allowed reducing operation temperature required for oxygen ion conduction through electrolyte from 1000°C down to 500°C (1-3). However, cell performance is limited because of the elevated cathode overpotential exhibited at these temperatures (3). Consequently, significant research effort has focused to overcome this issue in recent years. Adopted strategies include the development of mixed conductors (i.e. both electrons and ions conductors) and nano/microstructure optimization (2).

Several authors have reported cathode overpotential or proportional area specific resistance (ASR) decrease when reducing particle size to nanometer range (4-7). This enhancement was mostly ascribed to a larger surface/volume ratio which would increase

active sites for oxygen reduction reaction (ORR). Nevertheless, this explanation is not enough for all cases. For example, we have recently reported an ASR reduction of more than two orders of magnitude when diminishing particle size from 600 nm to 130 – 180 nm in $\text{La}_{0.4}\text{Sr}_{0.6}\text{Co}_{0.8}\text{Fe}_{0.2}\text{O}_{3-d}$ (LSCF) cathodes (4). These high-performance cathodes were prepared by chemical methods and present ASR values as low as $0.05 \text{ } \Omega\text{cm}^2$ at 600°C and $0.4 \text{ } \Omega\text{cm}^2$ at 450°C under air. This improvement can at least be partially attributed to the decrease of the particle size. However, it is interesting to note that these 130 – 180 nm particle-sized cathodes also present ASR values that are up to two orders of magnitude lower than those reported for a $\text{La}_{0.6}\text{Sr}_{0.4}\text{Co}_{0.95}\text{Fe}_{0.05}\text{O}_{3-d}$ cathode with 150 nm particle size (8). Since this reduction can't be solely explained by composition difference (9), it seems that some additional phenomenon occurs.

The aim of this work is to analyze the actual origin of ASR reduction of high performance nanostructured $\text{La}_{0.4}\text{Sr}_{0.6}\text{Co}_{0.8}\text{Fe}_{0.2}\text{O}_{3-d}$ cathodes prepared by chemical methods. Accordingly, ORR was investigated by electrochemical impedance spectroscopy (EIS) and nanostructure was characterized even at atomic level by transmission electron microscopy (TEM).

Experimental

$\text{La}_{0.4}\text{Sr}_{0.6}\text{Co}_{0.8}\text{Fe}_{0.2}\text{O}_{3-d}$ powder was prepared by acetic acid-based and hexamethylenetetramine (HMTA)-based methods (from now on called Acetate and HMTA). These powders were dispersed in an ink and deposited onto both sides of rectified $\text{Ce}_{0.9}\text{Gd}_{0.1}\text{O}_{2-d}$ (CGO) substrates with ~ 1.5 mm thickness by spin coating technique. Afterwards, these assemblies were heat treated at 900°C and 800°C for Acetate and HMTA method respectively, resulting in a symmetrical cell configuration used for electrochemical measurements. Particle sizes were determined by Scanning Electron Microscopy (SEM) while average crystallite size was determined by X-Ray diffraction (XRD). Cathodes prepared by HMTA method exhibit smaller particle (130 ± 30 nm) and average crystallite (27 ± 3 nm) sizes than cathodes prepared by Acetate (180 ± 40 nm and 40 ± 10 nm, respectively). Detailed preparation procedure and microstructural characterization of these cathodes were reported elsewhere (4,10).

Impedance measurements were performed in the $400\text{-}700^\circ\text{C}$ temperature range under pure oxygen and under synthetic air (20% O_2 -80% Ar mixture). Impedance spectra were recorded using a potentiostat/impedance analyzer Autolab (Eco Chemie BV) within the 10^{-3} - 10^6 Hz frequency range. Platinum grids, slightly pressed on electrodes, were used as current collectors. The total cathode area specific resistance (ASR) was determined following the procedure described in reference (10). All the impedance spectra were normalized taking into account the cathode geometric area ($= 0.88 \text{ cm}^2$).

Cathode nanostructure was characterized by TEM. Samples were prepared by focused ion beam (FIB)/lift-out technique as it was described in reference (11). Images were acquired with a Philips CM 200 UT microscope equipped with an ultra-twin objective lens, operated with a LaB_6 filament at 200 keV. The nominal resolution was 0.2 nm for the high resolution (HR-TEM) mode. The program ITEM© was used for mathematic treatment of the HR-TEM images.

Results and discussion

Study of the oxygen reduction reaction

Figures 1 and 2 show impedance spectra measured under air and under pure oxygen at different temperatures corresponding to LSCF/CGO/LSCF cells prepared by HMTA and Acetate methods, respectively. In both cases, the spectrum measured under oxygen at 400°C is quite similar to that measured at the same temperature under air. An extra contribution can be observed at low frequencies in the spectra measured under air for higher temperatures. The magnitude of the low frequency contribution augments as the temperature increases.

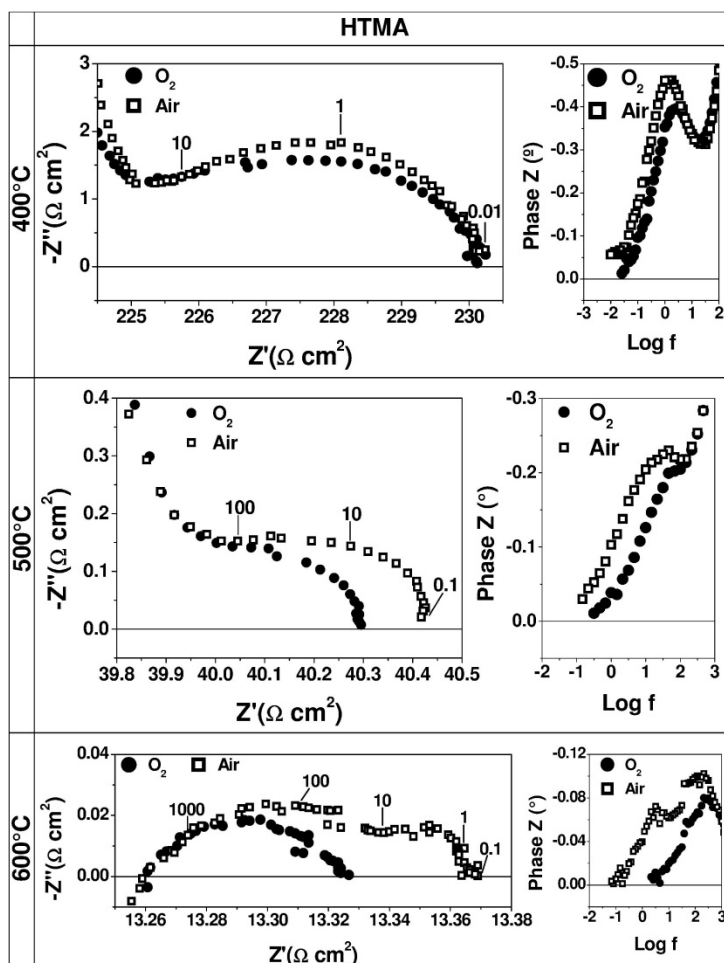


Figure 1. Nyquist (left) and Bode (right) plots of the impedance spectra recorded under air and pure oxygen at different temperatures for a LSCF/CGO/LSCF symmetric cell prepared by HMTA method. The numbers in the Nyquist plots indicates the frequency.

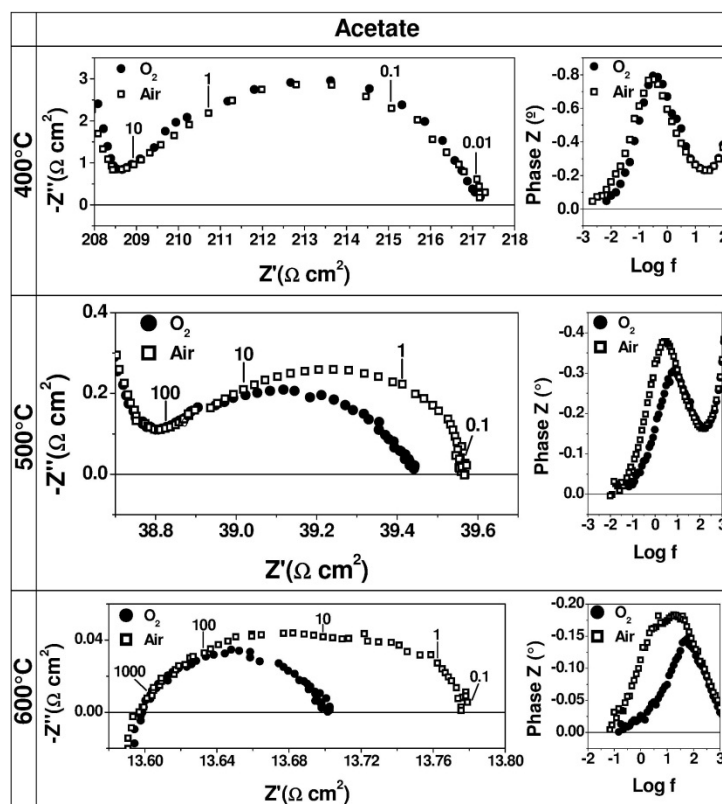


Figure 2. Nyquist (left) and Bode (right) plots of the impedance spectra recorded under air and pure oxygen at different temperatures for a LSCF/CGO/LSCF symmetric cell prepared by Acetate method. The numbers in the Nyquist plots indicates the frequency.

The Arrhenius plots of the total ASR values measured under pure oxygen and air for cathodes prepared by HMTA and Acetate methods are displayed in Figures 3a and b, respectively. These ASR values are within the lowest reported in literature (4,12) for SOFC cathodes and are up to more than two orders of magnitude lower than those reported for cathodes within LSCF family. The activation energy values under oxygen are 116 ± 5 kJ/mol and 108 ± 1 kJ/mol for HMTA and Acetate cathodes, respectively. These values are in agreement with the ~ 106 kJ/mol activation energy value reported for oxygen ionic conduction in $\text{La}_{0.6}\text{Sr}_{0.4}\text{Co}_{0.8}\text{Fe}_{0.2}\text{O}_{3-d}$ (13). This suggests that the high frequency contribution observed in the impedance spectra is related to the oxygen ion diffusion into the cathode bulk.

The low frequency contribution is dependent on the oxygen partial pressure since it is not observed in spectra measured under oxygen. Several authors have observed, at high temperatures and low partial pressures, a low frequency contribution related to oxygen gas-phase diffusion (12,14-16). ASR values related to this contribution are very small (i.e. in the order of $0.01 \text{ } \Omega\text{cm}^2$) and have slight dependence with the temperature (15,16). Table I summarized the ASR values related to the low frequency contribution for HMTA and Acetate cathodes. These values were determined as the difference between the ASR values at the low frequency end of the impedance spectra measured under air and under pure oxygen. ASR values related to the low frequency contribution in the 650-700°C range are within the expected ones for oxygen gas-phase diffusion and don't depend on the temperature.

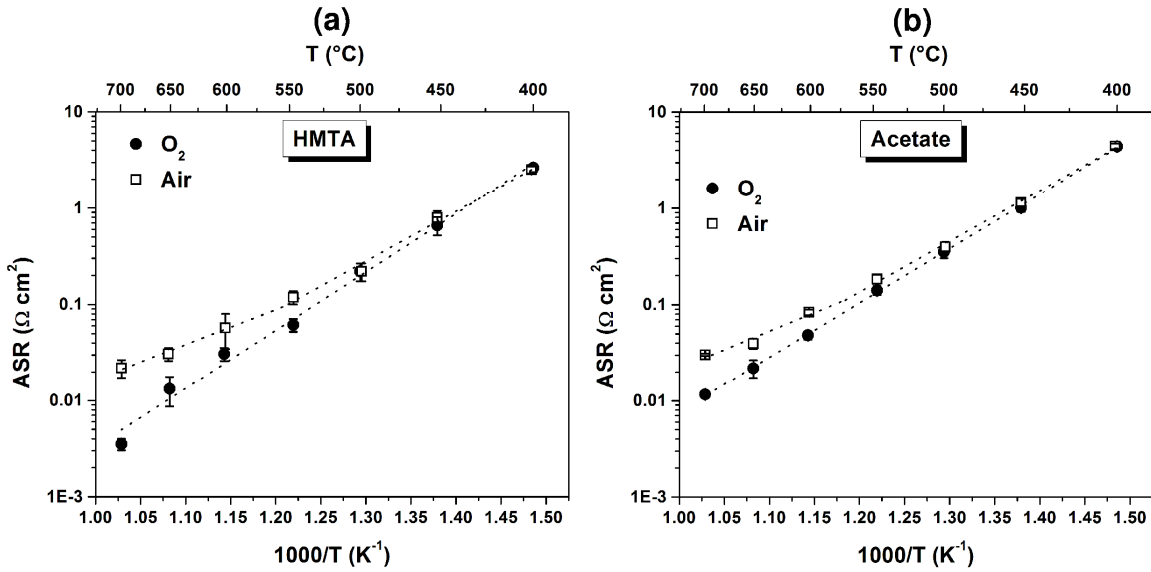


Figure 3. Arrhenius plots of the total ASR values measured under air and pure oxygen for LSCF cathodes prepared by (a) HMTA and (b) Acetate methods. The dotted lines represent the linear fitting of values.

TABLE I. ASR values corresponding to the extra low frequency contribution observed under air.

Temperature (°C)	HMTA	Acetate
450	0.26	0.29
500	0.058	0.083
550	0.050	0.061
600	0.026	0.042
650	0.017	0.019
700	0.017	0.019

The ORR at the nanostructured LSCF cathodes studied in this work can be described by the reaction model proposed by Grunbaum et al. for $\text{La}_{0.6}\text{Sr}_{0.4}\text{Co}_{0.8}\text{Fe}_{0.2}\text{O}_{3-d}$ cathodes prepared also by Acetate method but deposited by spray and heat treated at 1000°C (14). In that work, two contributions were identified by EIS: a high frequency one related to oxygen diffusion into LSCF material, and a low frequency one which evolves from dissociative oxygen adsorption at low temperature (i.e. 500°C) to oxygen gas-phase diffusion at high temperatures (i.e. 700°C). Accordingly, the higher ASR values observed at low temperatures (i.e. $\leq 600^\circ\text{C}$) for the low frequency contribution (see Table I) could be probably related to a co-limitation with oxygen adsorption.

In summary, the high frequency contribution (related to oxygen ion diffusion into cathode bulk) present ASR values that are up to more two orders of magnitude lower than those reported in literature (4,8), while the low frequency contribution (related to oxygen gas-phase diffusion) present ASR values that are similar to those reported in literature (23,32). Therefore, the low ASR values exhibited by our nanostructured $\text{La}_{0.4}\text{Sr}_{0.6}\text{Co}_{0.8}\text{Fe}_{0.2}\text{O}_{3-d}$ cathodes are originated in the enhancement of the oxygen diffusion into cathode bulk. Although this enhancement can be partially attributed to differences in the composition, the role of the cathode nanostructure should be considered. In view of that, we have investigated our cathodes by FIB-TEM technique.

The role of the cathode/electrolyte interphase

TEM and HR-TEM images at the cathode/electrolyte interphase show amazing results (see Figure 4a and b): the electrode layer not only covers a high percent of the electrolyte surface, but also the LSCF atomic planes match the orientation of the CGO grains (see also reference 11). This particular structure is possibly a consequence of the thermal treatment at moderated temperatures (i.e. 800 and 900°C for HMTA and Acetate methods, respectively) after the coating process. The slow phase formation may allow LSCF atoms to accommodate better to the substrate. This match explains in part the low ASR values exhibited by this samples; a pseudo-oriented interphase such as this one may facilitate the transfer of oxygen ions from the electrode towards the electrolyte by an oxygen vacancy conduction process.

It is worth to note that signs of material amorphization or redeposition due to the FIB preparation have not been observed. The interphase is the most reactive place of these samples because two very different materials coexist in a small area. Thus, if a radiation damage takes place, this zone should be preferentially affected with the Ga-ion sputtering process. The fact that a pseudo-oriented interphase could be imaged in many points, supports that the FIB did not induce an important damage into the atomic structure.

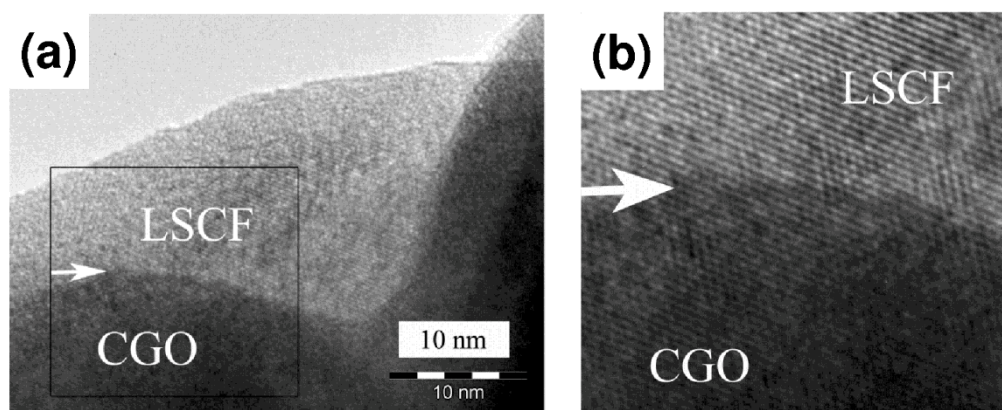


Figure 4. High resolution image at the LSCF/CGO interphase (white arrow). (a) Original image. (b) Square marked in (a) mathematically treated to highlight the orientation of the atomic planes at the interfacial zone; CGO is observed in a darker tone.

The role of the cathode nanostructure

The nanostructure from a $\text{La}_{0.4}\text{Sr}_{0.6}\text{Co}_{0.8}\text{Fe}_{0.2}\text{O}_{3-d}$ cathode prepared by HMTA can be seen in the HR-TEM image displayed in Figure 5a. Dark circles indicate a 2 nm and a 10-15 nm single-crystalline domains inside LSCF material while some crystalline disorder with amorphous appearance is observed in the rest of the material. It is worth to note that the appearance of this zone (LSCF) is different to that exhibited in the pore, indicating that this crystalline disorder belongs to LSCF material and not to the amorphous substrate which supports the sample. A similar appearance was observed in nanostructured $\text{La}_{0.4}\text{Sr}_{0.6}\text{Co}_{0.8}\text{Fe}_{0.2}\text{O}_{3-d}$ cathode prepared by Acetate method (see Figure 5b). This kind of nanostructure consisting of crystalline zones immersed in an amorphous phase where also observed in $\text{Ce}_{0.85}\text{Gd}_{0.15}\text{O}_{1.925}$ powders prepared by auto-combustion method (17) and in $\text{Ce}_{1-x}\text{Gd}_x\text{O}_{2-d}$ films deposited by spray pyrolysis (18).

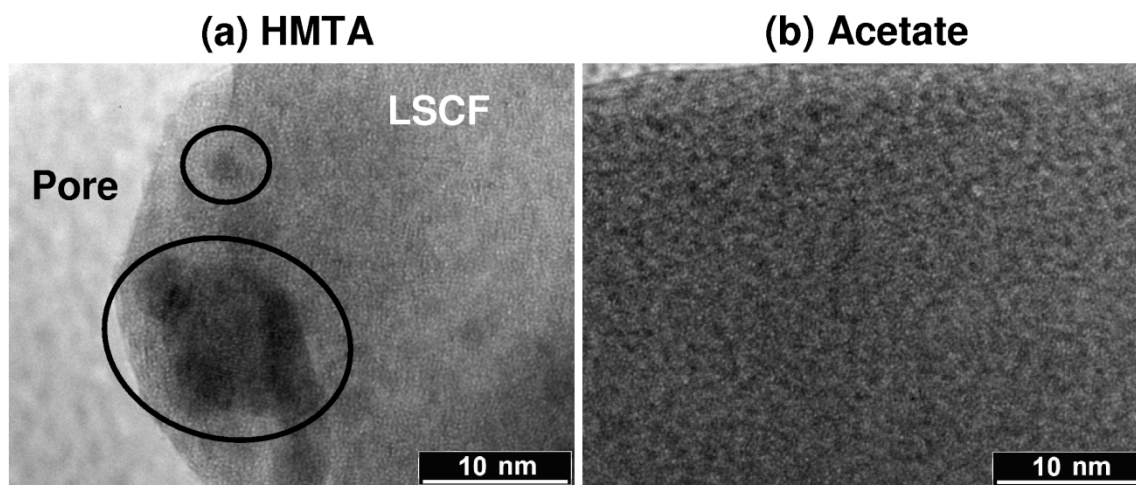


Figure 5. High resolution TEM images of the LSCF cathode showing well oriented single-crystalline domains included in a short range order matrix. (a) Samples synthesized by HMTA method. (b) Samples synthesized by the Acetate method.

Figure 6a shows a bright field (BF)-TEM image of a nanostructured $\text{La}_{0.4}\text{Sr}_{0.6}\text{Co}_{0.8}\text{Fe}_{0.2}\text{O}_{3-d}$ cathode prepared by HMTA method. Nanometric-sized dark zones represent nanocrystalline domains which are in diffraction condition since BF images are obtained selecting only the direct beam (19). This feature can be clearly visualized in the dark field (DF)-TEM image displayed in Figure 6b where bright zones correspond to the regions which are in diffraction conditions, and it is even more evident in HR-TEM resolution images from Figure 6c where the atomic columns inside the nanocrystals are observed.

A BF-TEM image from a nanostructured $\text{La}_{0.4}\text{Sr}_{0.6}\text{Co}_{0.8}\text{Fe}_{0.2}\text{O}_{3-d}$ cathode prepared by Acetate method is shown in Figure 7a while an electron diffraction pattern corresponding to LSCF material is displayed in Figure 7b. A diffuse ring, indicated as B in the Figure, is observed. Diffraction from disordered or amorphous regions typically originates this kind of ring (19). In addition, two intensive diffracted beams (indicating as A in the Figure) are observed over this ring. Both diffuse ring B and diffracted beams A correspond simultaneously to (1 1 0) and (1 0 4) planes of $\text{La}_{0.4}\text{Sr}_{0.6}\text{Co}_{0.8}\text{Fe}_{0.2}\text{O}_{3-d}$ (20) with a interplanar distance equal to 2.72 and 2.71 Å, respectively. A single crystalline zone extending tens of nm appears brighter in DF-TEM image when selecting diffracted beams A (see Figure 7c), indicating that this region is in diffraction condition. On the contrary, this zone darkens when part of diffusive ring B is selected (see Figure 7d), indicating that this zone is not in diffraction condition anymore while in the rest of the material several zones extending only few nm brighten, revealing numerous nanocrystals.

The excellent nanostructure exhibited by our cathodes consists on nanocrystals surrounded by zones with some degree of crystalline disorder. The ionic conductivity should be faster in these disordered regions with the consequent decrease of the ASR associated to oxygen diffusion, as it was reported by other authors for electrolyte materials (21-23). In that sense, simulations using a finite element model predicted a significant ASR decrease in nanostructured cathodes if the ionic conductivity of the grain boundary is more than 100 times higher than that of the bulk (24). It is worth to note that although different particle and average crystallite sizes were obtained by both preparation methods (4), nanostructured HMTA and Acetate cathodes exhibit comparable ASR

values (see Fig. 3). Therefore, the electrochemical performance improvement observed in both cathodes can be attributed to the similar nanostructure (i.e. nanocrystals surrounded by zones with some degree of crystalline disorder) present in them.

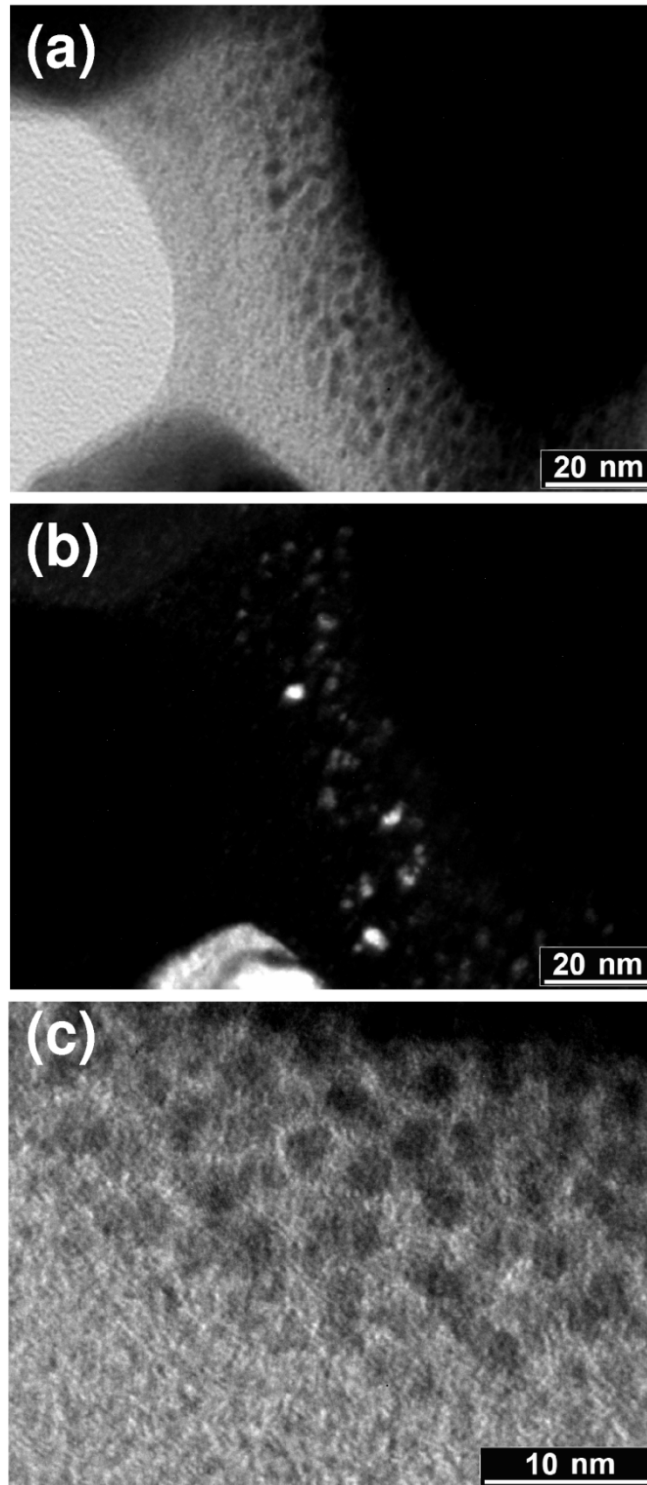


Figure 6. Bright field (a), dark field (b) and high resolution (c) images of a LSCF cathode prepared by HMTA, showing the nanocrystalline domains (in average smaller than 5 nm). In (a) and (b) also a bigger domain (approx. 50 nm) can be observed in the bottom left edge.

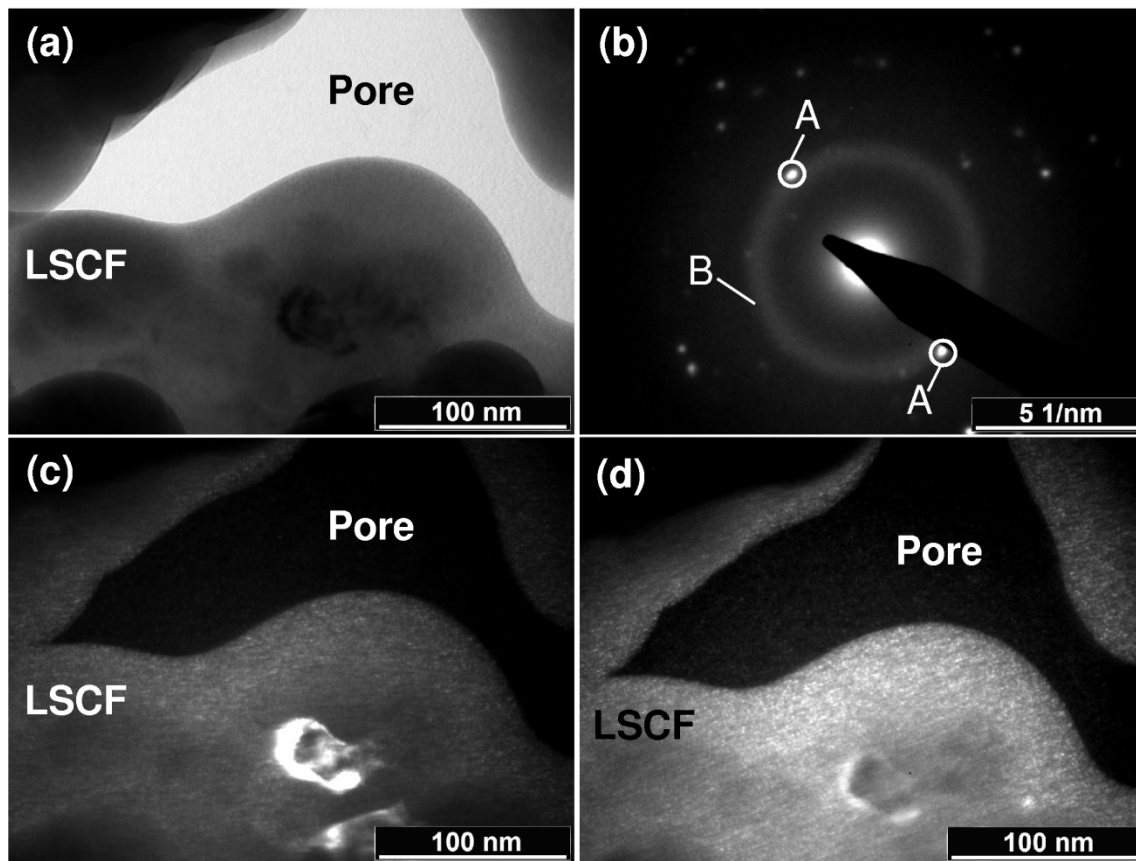


Figure 7. TEM image (a) and diffraction pattern (b) using all transmitted and diffracted electrons. Dark field images obtained using the beams marked in figure (b) as “A” (c) and the ring marked as “B” (d).

Conclusions

ASR values of nanostructured $\text{La}_{0.4}\text{Sr}_{0.6}\text{Co}_{0.8}\text{Fe}_{0.2}\text{O}_{3-d}$ cathodes prepared by HMTA and Acetate methods are within the lowest reported in the literature and are up to more than two orders of magnitude lower than cathodes with similar composition. The lower ASR values exhibited by these nanostructured LSCF cathodes are originated by an enhancement of oxygen vacancy diffusion into cathode bulk. This improvement is the result of the excellent cathode nanostructure consisting on nanocrystals surrounded by zones with some degree of crystalline disorder.

Acknowledgments

Nicolás Grunbaum, Richard Wirth, Liliana Mogni, Diego Lamas and Alfredo Tolley are acknowledged for useful discussions. This work was funded by University of Cuyo, CONICET, CNEA and ANPCyT-PICT.

References

1. B. C. H. Steele and A. Heinzl, *Nature*, **414**, 345 (2001).
2. A. J. Jacobson, *Chem. Mat.*, **22**, 660 (2010).
3. E. Ivers-Tiffée, A. Weber and D. Herbstritt, *J. European Ceramic Soc.*, **21**, 1805 (2001).
4. L. Baqué, A. Caneiro, M. S. Moreno and A. Serquis, *Electrochemistry Comm.*, **10**, 1905 (2008).
5. J. Yoon, S. Cho, J.-H. Kim, J. H. Lee, Z. Bi, A. Serquis, X. Zhang, A. Manthiram and H. Wang, *Adv. Funct. Mater.*, **19**, 1 (2009).
6. M. G. Bellino, J. G. Sacanell, D. G. Lamas, A. G. Leyva and N. E. Walsöe de Reca, *J. Am. Chem. Soc.*, **129**, 3066 (2007).
7. J. M. Serra, H.-P. Buchkremer, *J. Power Sources*, **172**, 768 (2007).
8. F. Deganello, V. Esposito, M. Miyayama and E. Traversa, *J. Electrochem. Soc.*, **154**, A89 (2007).
9. Y. Teraoka, H. M. Zhang, K. Okamoto and N. Yamazoe, *Mat. Res. Bull.*, **23**, 51 (1988).
10. L. Baqué, E. Djurado, C. Rossignol, D. Marinha, A. Caneiro and A. Serquis, *ECS Trans.*, **25**, 2473 (2009).
11. A. L. Soldati, L. Baqué, H. Troiani, C. Cotaro, A. Schreiber, A. Caneiro and A. Serquis, *Int. J. Hydrogen Energy*, **36**, 9180 (2011).
12. J. Hayd, H. Yokokawa and E. Ivers-Tiffée, *J. Electrochem. Soc.*, **160**, F351 (2013).
13. D.-P. Huang, Q. Xu, W. Chen, H. Wang and R.-Z. Yuan, *J. Inorg. Mater.*, **20**, 133 (2005).
14. N. Grunbaum, L. Dessemond, J. Fouletier, F. Prado, L. Mogni and A. Caneiro, *Solid State Ionics*, **180**, 1448 (2009).
15. S. P. Yoon, S. W. Nam, J. Han, T.-H. Lim, S.-A. Hong and S.-H. Hyun, *Solid State Ionics*, **166**, 1 (2004).
16. A. J. Darbandi and H. Hahn, *Solid State Ionics*, **180**, 1379 (2009).
17. N. K. Singh, P. Singh, M. K. Singh, D. Kumar and O. Parkash, *Solid State Ionics*, **192**, 431 (2011).
18. J. L. M. Rupp, C. Solenthaler, P. Gasser, U. P. Muecke and L. J. Gauckler, *Acta Materialia*, **55**, 3505 (2007).
19. D. B. Williams and C. B. Carter, *Transmission electron microscopy: a textbook for materials science*, Plenum Press (1996).
20. F. Prado, N. Grunbaum, A. Caneiro and A. Manthiram, *Solid State Ionics*, **167**, 147 (2004).
21. M. G. Bellino, D. G. Lamas and N. E. Walsöe de Reca, *Adv. Funct. Mater.*, **16**, 107 (2006).
22. P. Heitjans and S. Indris, *J. Phys.: Condens. Matter*, **15**, R1257 (2003).
23. H. L. Tuller, *Solid State Ionics*, **131**, 143 (2000).
24. W. Preis, E. Bucher and W. Sitte, *Fuel Cells*, **12**, 543 (2012).